Nature Communications

https://doi.org/10.1038/s41467-026-69992-y

Article in Press

Interplate rheological contrast revealed by asymmetric deformation after the 2023 Kahramanmaraş earthquakes

Received: 3 August 2025

Accepted: 13 February 2026

Cite this article as: Liu, J., Jónsson, S., Li, X. *et al.* Interplate rheological contrast revealed by asymmetric deformation after the 2023 Kahramanmaraş earthquakes. *Nat Commun* (2026). https://doi.org/10.1038/s41467-026-69992-y

Jihong Liu, Sigurjón Jónsson, Xing Li, Wenqian Yao & Yann Klinger

Interplate rheological contrast revealed by asymmetric deformation after the 2023 Kahramanmaraş earthquakes

Jihong Liu[1], Sigurjón Jónsson[1,*], Xing Li[2], Wenqian Yao[3,4], Yann Klinger[3]

[1]King Abdullah University of Science and Technology (KAUST), Thuwal, Saudi Arabia
[2]Bureau of Economic Geology, The University of Texas at Austin, Austin, Texas, U.S.A.
[3]Université Paris Cité, Institut de Physique du Globe de Paris, CNRS, F-75005 Paris, France
[4]Institute of Surface-Earth System Science, School of Earth System Science, Tianjin University, Tianjin, China

[*]Corresponding author: Sigurjón Jónsson (sigurjon.jonsson@kaust.edu.sa)

Abstract

Postseismic surface deformation offers key insights into subsurface lithospheric rheology and earthquake fault behavior, yet geodetic data often fail to capture its full complexity. Here, we use satellite radar images to derive time series of three-dimensional surface displacements following the 2023 Kahramanmaraş (Türkiye) earthquakes. The results show strong spatial and temporal deformation asymmetry across the East Anatolian Fault with the stiffer Arabian lithosphere exhibiting slower deformation decay than the Anatolian side. The temporal asymmetry excludes elastic afterslip from being the main postseismic process and instead the postseismic response is dominated by asymmetric viscoelastic relaxation as well as poroelastic rebound. These findings underscore the importance of both temporal and three-dimensional spatial deformation data in advancing understanding of post-earthquake recovery processes and subsurface lithospheric structure.

Introduction

Postseismic processes following major earthquakes, including viscoelastic relaxation, poroelastic rebound, and afterslip, are of paramount importance for understanding lithospheric rheology, fault slip characteristics, and regional tectonic movements[1-3]. One of the most direct manifestations of these postseismic processes is surface deformation, which can be measured using geodetic techniques such as interferometric synthetic aperture radar (SAR, InSAR) and global navigation satellite system (GNSS). While different postseismic processes reflect the properties of the subsurface medium from distinct perspectives, the surface deformation measured results from a combination of all these different postseismic processes. Consequently, significant efforts have been made to distinguish between these processes. For instance, by leveraging prior information or simplified assumptions, studies often focus on a specific postseismic process while neglecting other secondary processes[4-6]. Alternatively, based on the spatiotemporal characteristics of the different postseismic processes, attempts have been made to sequentially separate these processes from the observed surface deformation[7-9]. However, accurately distinguishing between different postseismic processes remains highly challenging due to the often incomplete geodetic coverage of the affected area or the inability to reveal the full-dimensional (temporal and 3D spatial) surface deformation. This is particularly true for the highly complex 2023 Kahramanmaraş earthquakes[10,11].

The Kahramanmaraş earthquake sequence on February 6, 2023, comprised two major events with magnitude 7.8 and 7.6, occurring at the boundary between the Arabian and Anatolian plates, i.e., on the East Anatolian fault (EAF) and Sürgü fault, respectively[12]. These two earthquakes were separated by only 9 hours in time and approximately 90 kilometers in distance, with a total fault rupture length extending 500 kilometers (Fig. 1). The seismic activity released the accumulated stress along EAF due to the westward extrusion of the Anatolian Plate[13,14]. The long-term tectonic evolution of Anatolian Plate has been interpreted by the westward tectonic escape driven by northward movement of Arabian Plate[15,16], with the EAF acting as a key transform boundary accommodating this motion[17-20]. Later geodynamic models further suggested that this escape is sustained by large-scale mantle flow coupling westward slab pull in the Aegean Sea[21-23]. Across the EAF, the Arabian lithosphere collides into Anatolia at the EAF, and is thought to be relatively rigid and homogeneous[24]. Conversely, the Anatolian Plate has formed through multiple subduction and collision events, and is still deforming under a variety of tectonics processes from east to west[25,26]. Additionally, the pronounced lateral heterogeneity across the EAF is highlighted by the significant differences in the thickness of subsurface structural layers[27-29] in the region's seismic structure. These complex geological settings and the associated seismogenic faults suggest that the postseismic deformation pattern is highly intricate.

In this study, we combined nearly two years of postseismic Sentinel-1 images with time-series InSAR[30,31] and burst overlap interferometry (BOI)[32,33] methods to capture the full-dimensional (temporal, east-west, north-south, and vertical) deformation following the earthquakes. The availability of such comprehensive surface deformation data enables discrimination of the distinct postseismic processes, i.e., viscoelastic relaxation in the lower crust and upper mantle, poroelastic rebound of the crust, and afterslip on and below the coseismic fault slip. This capacity stems from the dissimilar contributions of these mechanisms to different components of the surface deformation[34], as well as from the notable temporal and spatial deformation asymmetry observed in this case.

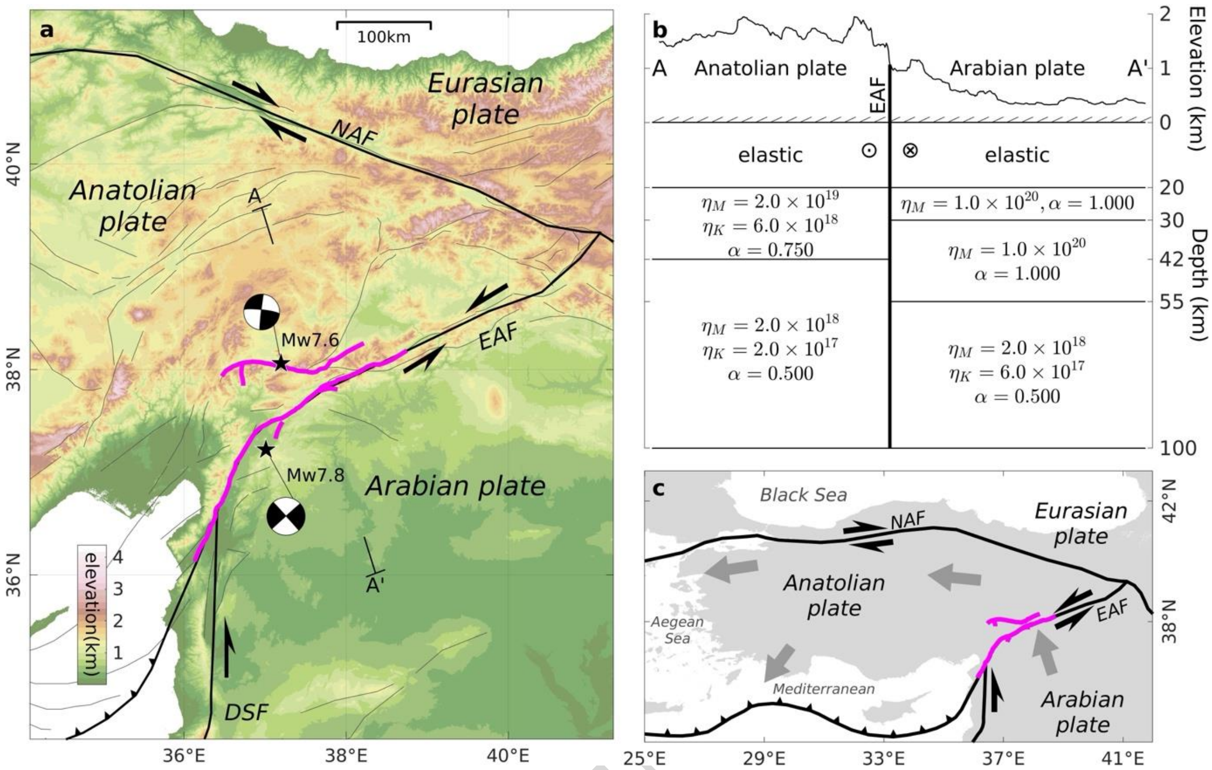

Fig. 1. **Tectonic setting around the 2023 Kahramanmaraş earthquakes. a** Map of the magnitude 7.8 and 7.6 Kahramanmaraş earthquake surface ruptures (magenta lines)[35] of February 6, 2023. The mainshock epicenter locations (black stars), focal mechanism solutions (beach balls)[36], and main faults (black lines) are shown. EAF, East Anatolian fault; NAF, North Anatolian fault; DSF, Dead Sea fault. **b** Elevation along profile A-A' (shown in **a**) and the layered structures with corresponding viscoelastic parameters across the EAF used for our viscoelastic modeling. η_M and η_K are the steady-state (Maxwell body) and transient (Kelvin body) viscosities of the Burgers modeling material, respectively, μ_K and μ_M are the corresponding shear modulus, and α is the ratio between the effective and the unrelaxed shear modulus (i.e., $\alpha = \mu_K/(\mu_K + \mu_M)$), where $\alpha = 1.0$ is a pure Maxwell body[37]. **c** The tectonic plates around the 2023 Kahramanmaraş earthquakes. Grey arrows show the approximate horizontal plate movement relative to the Eurasian plate[38]. The shaded relief background map was derived from the shuttle radar topography mission (SRTM) 3-arc seconds data[39].

Results

Time series of three-dimensional postseismic displacements

Using time-series InSAR and BOI methods, we obtained four relatively independent postseismic displacement observations with distinct geometric differences from both ascending and descending orbits in the line-of-sight (LOS) and azimuth directions (Materials and Methods). To ensure complete coverage of the deformation area, both ascending and descending datasets include three adjacent orbital tracks (each with a swath width of 250 km), with each track consisting of 4-5 frames (Supplementary Fig. 1). The InSAR LOS observations (Supplementary Fig. 2) provide spatially continuous displacement maps in the east-west (EW) and vertical directions. The BOI observations, on the other hand, are only available in burst overlap areas (Supplementary Fig. 2), and the resulting north-south (NS) displacement is therefore not entirely spatially continuous.

Nevertheless, BOI complements InSAR by revealing the overall characteristics of postseismic deformation in the NS direction[40,41]. To remove secular interseismic tectonic signals from the postseismic displacement field, we also processed Sentinel-1 data from 2015-2023 using both time-series InSAR and BOI methods (Supplementary Fig. 3). Comparison with publicly available GNSS solutions[42,43] exhibits root-mean-square (RMS) differences of 17 mm, 11 mm, and 11 mm between the GNSS and postseismic InSAR cumulative displacements in the EW, NS, and vertical directions, respectively (Supplementary Fig. 4).

The postseismic three-dimensional (3D) displacements (Figs. 2a, 2c, and 2e) indicate that the deformation characteristics align well with the expected postseismic response from the left-lateral strike-slip earthquakes. Horizontal deformation dominates the postseismic surface displacement, reaching magnitudes of up to 15 cm within two years. Regarding the near-field horizontal deformation, most areas exhibit a smooth cross-fault transition (except at the northeastern ends of the two primary fault ruptures), suggesting a limited contribution from shallow afterslip. In terms of vertical deformation, a notable characteristic is the presence of extensive scale (~200 km) uplift and subsidence (~5 cm) respectively north and south of the EAF. Compared to the coseismic deformation[35], the spatial extent of the postseismic deformation is significantly larger, suggesting a substantial contribution from processes deeper than the coseismic fault slip[44].

A pronounced spatiotemporal asymmetry is observed between the Arabian and Anatolian plates in the postseismic EW displacement field (Fig. 2). The mechanically weaker Anatolian plate exhibits higher and more spatially concentrated deformation, whereas on the Arabian side lower deformation is distributed over a broader area. To fit the temporal evolution of EW deformation, we applied a logarithmic function (i.e., $d = a \cdot log_{10}(1 + t/T)$)[45,46]. The results reveal that the decay time T (Figs. 2a and 2j) on the Arabian plate is systematically larger than that on the Anatolian side, implying that, compared to the Anatolian Plate, the postseismic deformation of the Arabian Plate originates from a more prolonged subsurface process.

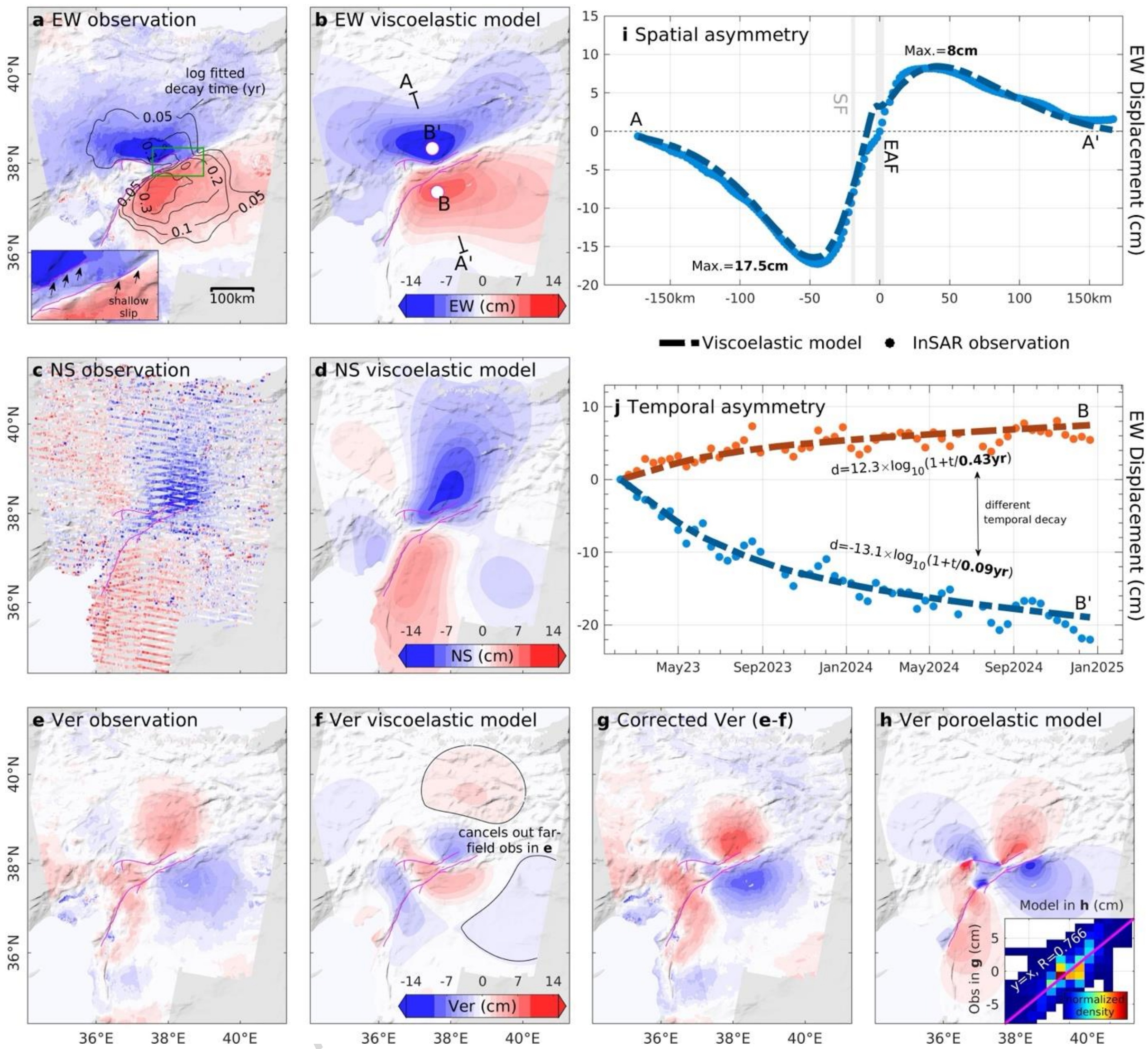

Fig. 2. **Observed and modeled surface displacements.** **a**, **c**, and **e** are respectively the cumulative east-west (EW), north-south (NS), and vertical (Ver) displacements from February 2023 to December 2024. **b**, **d**, and **f** are the corresponding viscoelastic modeling displacements. Contours in **a** are the fitted logarithmic decay times from EW displacement time series highlighting slower postseismic motions on the Arabian side. The inset panel provides a zoom-in view of the green box with the limited shallow afterslip observed near the northeastern end of the ruptures. The displacements along profile A-A’ are shown in **i** and displacement time series of points BB’ are shown in **j**, highlight the spatial and temporal decay asymmetry of postseismic deformation across the East Anatolian Fault (EAF). SF, Sürgü fault. **g** is the vertical observation corrected for viscoelastic model displacements, where the viscoelastic prediction cancels out the vertical signals far away from the fault, leaving the residual vertical deformation concentrated in the near-field. **h** is the best fit of poroelastic model to **g** with the inset panel showing the correlation between **g** and **h**. The residual maps comparing the model predictions with the 3D observations are shown in Supplementary Fig. 5. The shaded relief background map was derived from the shuttle radar topography mission (SRTM) 3-arc seconds data[39].

Postseismic Modeling

Postseismic deformation that is spatially asymmetric across a fault could potentially be caused by elastic afterslip if the lithospheric structure of the two fault sides is different. However, the observed temporal asymmetry cannot be explained by elastic afterslip, as such afterslip would yield the same deformation decay times on both sides. For that reason, we model the postseismic deformation as a combination of viscoelastic relaxation and poroelastic rebound using the time series of 3D postseismic displacements. For the viscoelastic modeling, both EW and NS displacements are used. Given that near-field deformation could be influenced by shallow fault slip, we conducted an independent test by searching for the optimal model parameters using only data beyond 50 km (approximately twice the seismogenic depth[47-49]). The results indicate that the inclusion of near-field observations has an insignificant impact on the optimal model solution (Supplementary Figs. 6-7). In addition, observed vertical displacements were excluded from the viscoelastic modeling process, as they primarily stem from poroelastic rebound, a mechanism we subsequently address. While lower crustal relaxation can generate vertical deformation signals resembling those observed, prioritizing the fit to vertical deformation leads to a quite poor fit in the horizontal component (Supplementary Fig. 8).

We accounted for viscoelastic relaxation in both the lower crust and upper mantle using information about the subsurface layered structure (Fig. 1b) derived from available seismic velocity data[50]. The shear-wave velocity v_s profile beneath the Arabian Plate shows anomalously high values (~4.6 km/s) at 30-55 km depths[24], suggesting a mechanically strong layer. We assigned a high viscosity of 1×10^{20} Pa·s to this layer, having tested alternative viscosities and examined scenarios where the Arabian and Anatolian Plates share identical layered structures (Supplementary Fig. 9). These tests confirmed higher rigidity of this layer compared to adjacent strata. Through grid search optimization (Supplementary Fig. 6), we determined viscosities for other layers using the PSGRN/PSCMP software (Materials and Methods) (Fig. 1b), revealing that the Arabian Plate's lower crust ($\eta_M = 1 \times 10^{20}$ Pa·s) is substantially more rigid than the Anatolian Plate's ($\eta_M = 2 \times 10^{19}$ Pa · s, $\eta_K = 6 \times 10^{18}$ Pa · s). In the upper mantle, the steady-state viscosity η_M is similar on both sides ($\eta_M = 2 \times 10^{18}$ Pa · s) except for the strong Arabian layer at 30-55 km, but a lower transient viscosity ($\eta_K = 2 \times 10^{17}$ Pa · s) representing faster postseismic relaxation is found on the Anatolian side compared to the Arabian plate ($\eta_K = 6 \times 10^{17}$ Pa · s). This lateral heterogeneity in structure and viscosity correlates well with observed spatiotemporal asymmetry of EW displacements. The viscoelastic model predictions achieve an excellent fit to the EW and NS deformation fields, as well as their temporal evolution (Figs. 2 and Supplementary Fig. 10), confirming the validity of the viscoelastic model and suggesting a minimal contribution from afterslip (Supplementary Figs. 11-12).

The viscoelastic model, while providing a good fit to horizontal deformation, still exhibits significant residuals in the vertical component (Fig. 2g). This indicates that poroelastic rebound also plays an important role in the postseismic deformation. Based on the coseismic slip model (Fig. 3a), we isolated the contribution of poroelastic rebound by computing the difference in forward-modeled vertical surface deformation under undrained and drained Poisson's ratios in the Green's function relating slip to surface displacement. Our analysis reveals that during the postseismic period, the highest correlation coefficient of 0.76 between model predictions and observations (Fig. 2h) is achieved when the difference in undrained and drained Poisson's ratios reaches 0.1-0.13 (Fig. 3d). Although the vertical residuals from the poroelastic rebound model remain non-negligible (Supplementary Fig. 5c), the model successfully captures the first-order pattern of the observed deformation.

Absolute values of Poisson's ratio under undrained and drained conditions are usually considered in poroelastic rebound modeling[4,51,52]. However, we argue that specifying absolute values is unnecessary as long as the chosen value falls within a reasonable range (e.g., 0.2-0.35). Poroelastic rebound-induced vertical deformation is more sensitive to the change in Poisson's ratio between the undrained and drained states than to their absolute values (Fig. 3c). While different assumptions regarding the undrained Poisson's ratio could theoretically influence the estimated coseismic slip, and consequently the poroelastic deformation, we find this effect to be negligible (Fig. 3b). Furthermore, our poroelastic rebound modeling indicates lateral heterogeneity across the EAF, with Poisson's ratio changes of 0.13 on the Arabian side and 0.1 on the Anatolian side (Fig. 3d). This contrast results in slightly larger poroelastic vertical rebound on the Arabian plate. A Poisson's ratio change $\Delta\nu = \nu_u - \nu_d$ as large as 0.1-0.13 has rarely been reported in previous case studies, where typical variations are only about half that magnitude (~0.05)[4,51]. This suggests substantial coseismic and then postseismic change in crustal material properties in the region caused by these two large earthquakes, particularly within the stiffer Arabian plate.

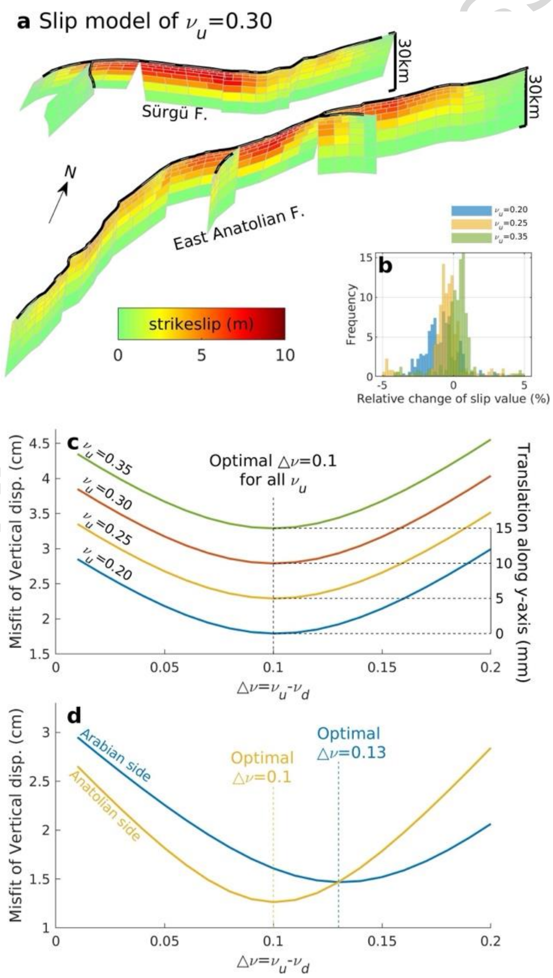

Fig. 3. **The effect of coseismic undrained Poisson's ratio ν_u on poroelastic modeling. a** The coseismic strike-slip model[35] used in the poroelastic modeling with $\nu_u = 0.30$. **b** The change of slip values for different Poisson's ratios ν_u relative to the slip value in **a** with $\nu_u = 0.30$. **c** The misfit between observed vertical displacements and the poroelastic modeling prediction under different undrained Poisson's ratios ν_u and Poisson's ratio differences $\Delta\nu$. ν_d is the postseismic

drained Poisson's ratio. For clarity, results of different ν_u in **c** are translated along y-axis. **c** clarifies that changes in Poisson's ratio are more important than its absolute value. Noted that the misfit in panel **c** is computed using data from both sides of the East Anatolian Fault. **d** is similar to **c**, but the misfit is calculated separately for the Arabian and Anatolian sides to account for the lateral heterogeneity across the fault.

Discussion

While it is normally challenging to fully separate crustal afterslip from viscoelastic relaxation[53], the spatiotemporal asymmetry (Figs. 2a, 2i and 2j) in our full-dimensional postseismic deformation results indicates viscoelastic relaxation is the dominant postseismic deformation mechanism for this event. As mentioned above, the spatial asymmetry could arise from either lateral variation in the viscosity of the lower crust and upper mantle, or from afterslip occurring within an elastic crust of heterogeneous stiffness. However, the observed asymmetric temporal decay of deformation is consistent only with contrasting viscosities across the fault, as elastic afterslip would generally induce simultaneous surface motion on both sides of the fault, resulting in symmetric decay. Therefore, the unique spatiotemporal asymmetric deformation pattern excludes afterslip from being the key postseismic process, in contrast to previously published results[43], and strongly points to viscoelastic relaxation as the primary postseismic deformation mechanism.

Previous studies of asymmetric deformation associated with large strike-slip earthquakes have predominantly focused on spatial asymmetries. Notable examples include the coseismic deformation of the 1997 Manyi and 1999 Hector Mine earthquakes[54-56], and the postseismic deformation of the 2001 Kokoxili and 2021 Maduo events[57-60]. In these cases, observed asymmetries have commonly been attributed to variations in fault dip[55,56] or contrasts in elastic properties across the fault[54]. Alternatively, based on limited geodetic displacement observations, differences in viscosity on either side of the fault have been proposed to explain the asymmetry, rather than afterslip, by leveraging the distinct temporal scales of afterslip and viscoelastic relaxation[57,58]. However, these studies have either overlooked the temporal asymmetry or been unable to analyze it due to limitations in available geodetic observations, highlighting the unique perspective offered by the case presented here through the full-dimensional postseismic deformation data.

Furthermore, according to rate-and-state friction theory, afterslip typically occurs within the brittle upper crust at moderate temperatures (350-450°C)[61,62]. At greater depths, where temperatures are higher (i.e., in the lower crust and upper mantle), postseismic deformation is primarily governed by viscoelastic flow[5,6,63]. Numerous studies have also shown that afterslip is generally confined to the upper crust and transitional zones[58,64,65]. Although a kinematic afterslip model can achieve an adequate fit to the observed data (Supplementary Figs. 11 and 13), such a model has significant physical inconsistencies with unreasonable amounts of afterslip[66] extending to depths of as much as 50 km without showing signs of decaying with depth (Supplementary Fig. 11c), despite that the lower crust extends to only ~40 km in this region.

That being said, we do not entirely rule out some contributions of postseismic afterslip. Since afterslip and viscoelastic relaxation in the lower crust may produce similar surface deformation[67], it is difficult to fully distinguish between them using geodetic observations within the first two years following an earthquake, especially when the lower-crustal contribution, from either afterslip or viscoelastic relaxation, is minor. In our viscoelastic model, the viscosity of the lower crust is an order of magnitude higher than that of the upper mantle, suggesting that the lower crust plays a minimal role in postseismic surface deformation during the first two years. Even if all the lower-crustal deformation was attributed to afterslip rather than viscoelastic relaxation, the lower-crustal contribution would be relatively minor (Supplementary Fig. 14) and the dominant postseismic signal within the first two years would still be primarily governed by upper mantle viscoelastic relaxation.

Previous studies on the viscoelastic properties of the Anatolian Plate have primarily focused on the North Anatolian fault (NAF), largely associated to the series of major earthquakes that occurred there in the past century[68,69]. Studies of the 1999 Izmit earthquake indicate that the viscosity of the lower crust near the NAF is approximately 10^{19} Pa·s[70,71], consistent in magnitude with our findings for the East Anatolian Fault (EAF) region. Studies of the upper mantle viscosity near the NAF, however, suggest that the viscosity is higher than that of the lower crust[8], which contrasts our findings for the Anatolian Plate near the EAF, where the lower crust is stronger than the upper mantle. This difference may be attributed to the interaction between the Arabian and Anatolian plates near the EAF, which results in a softer and hotter asthenosphere in this region[72-74]. In comparison, fewer studies have focused on the viscoelastic properties of the Arabian Plate due to its relative stability[75,76]. Our results reveal a strong lower crust and uppermost mantle beneath the Arabian Plate, suggesting that as it moves northward, the softer Anatolian Plate gives way resulting in more deformation. These processes may also involve the delamination of rigid lithospheric segments and crustal flow[77,78], contributing to localized surface uplift, the formation of the Eastern Anatolian Plateau, and the westward motion of the Anatolian Plate.

In conclusion, we have utilized time-series of three-dimensional surface displacements derived from satellite SAR images to reliably demonstrate that the primary postseismic deformation mechanism following the 2023 Kahramanmaraş earthquakes is viscoelastic relaxation with notable contributions from poroelastic rebound, but with afterslip playing only a minor role. This distinction is enabled by full-dimensional (temporal and 3D spatial) surface deformation measurements and the observed temporal asymmetry in the deformation. Specifically, our findings reveal significant lateral heterogeneity in the subsurface structure of the EAF zone, with the Anatolian Plate exhibiting a softer lower crustal structure and faster transient relaxation of the upper mantle compared to the Arabian Plate. For major strike-slip earthquakes like the 2023 Kahramanmaraş earthquakes occurring along plate boundaries, our comprehensive time-series of three-dimensional surface deformation analysis helps to clarify the dominant deformation mechanisms during the postseismic phase and provides valuable constraints on the subsurface rheological structure.

Methods

Interferometry of synthetic aperture radar images

To capture the postseismic deformation from the 2023 Kahramanmaraş earthquakes, we employed time-series InSAR and BOI (Burst Overlap Interferometry) techniques to derive surface displacements along both the satellite line-of-sight (LOS) and azimuth directions. The Sentinel-1 dataset used in this study includes three ascending and three descending tracks, each comprising 4-5 frames. We utilized both short-temporal-baseline interferograms and interferograms with longer temporal baselines (around one year) but short spatial baselines (e.g., less than 15 meters) (Supplementary Fig. 15). Preprocessing steps, including SAR image co-registration, interferogram generation, and phase unwrapping, were performed using GAMMA software.

To derive the LOS displacement from time-series InSAR data with improved signal-to-noise ratio, we first applied a multi-looking process with a 30×10 (range×azimuth) window to the interferograms. An adaptive filtering technique was then used, with a filter factor of 0.4 and a window size of 64. Phase unwrapping was subsequently performed using the Minimum Cost Flow (MCF) method. After unwrapping, we employed the Small Baseline Subset (SBAS) technique to invert the time-series deformation for each satellite track. Due to differences in temporal sampling between tracks, the time reference of the time-series deformation for each track also varies. To unify the temporal reference across tracks and to account for possible period non-tectonics signals, we fitted each track's time-series deformation using the empirical function $d = a * log_{10}(1 + t/T_1) + b * sin(2\pi t/T_2 + \emptyset_0) + c$ (Supplementary Fig. 16). By removing the fitted sinusoidal component and the constant offset from the original displacement data, we isolate the postseismic displacement time series (blue markers), referenced to the moment immediately after the earthquake. Although early postseismic deformation tends to be large and difficult to fit accurately, our results show that the cumulative deformations from different tracks are generally consistent within overlapping regions and are also in good agreement with GNSS observations (Supplementary Fig. 4). This consistency supports the effectiveness of our processing strategy. To further derive east-west and vertical time-series deformation from ascending and descending LOS observations, we interpolated each track's time-series data onto a unified temporal sampling grid (Supplementary Fig. 16). For each epoch, we then applied a simple least-squares method to estimate the east-west and vertical components by neglecting north-south deformation[79]. Previous studies have shown that while this approach yields accurate east-west deformation, the presence of true north-south deformation can introduce systematic errors into the derived vertical deformation[80]. This is one of the reasons we chose to use only east-west deformation in our viscoelastic modeling. To obtain more accurate vertical deformation fields, we corrected the vertical component using the modeled north-south deformation (Fig. 2d) from our viscoelastic forward model[80].

The BOI processing is generally similar to the workflow of time-series InSAR. After generating Single Look Complex (SLC) images from Sentinel-1 data in the Burst Overlap (BO) region using GAMMA software, we performed differential interferometric processing. For both forward- and backward-looking interferograms in the BO region, the same topographic phase was applied for terrain correction. Prior to differencing the forward- and backward-looking interferograms to obtain the BOI interferogram, we applied adaptive filtering to enhance the signal-to-noise ratio of the resulting BOI interferogram. Following the generation of the BOI interferogram, we employed the SBAS method to invert the time-series deformation along the azimuth direction. To derive the north-south (NS) deformation in the BO region, we corrected for the east-west (EW) displacement (i.e., Fig. 2a) in the BOI azimuth displacement based on the formula of $BOI = \sin(\alpha) \cdot EW + \cos(\alpha) \cdot NS$ with α the azimuth angle of SAR satellite.

The ascending and descending LOS and azimuth displacements derived from the above data processing contain both postseismic deformation and long-term secular deformation. To eliminate the influence of secular deformation on the analysis of the postseismic process, we obtained interseismic displacements by processing Sentinel-1 images spanning 2015 to 2023. The processing steps for the interseismic data were largely consistent with those used for the postseismic period. Notably, a Mw 6.8 earthquake occurred along the East Anatolian Fault (EAF) on January 24, 2020[81]. To remove the coseismic deformation introduced by this event from the estimation of the interseismic deformation rate, we fitted the interseismic time series using a Heaviside step function (see Supplementary Fig. 17). In this analysis, we did not account for the postseismic deformation from this event. Given the moderate magnitude of the earthquake and the relatively long duration of our time series (approximately 8 years), the postseismic deformation contribution of this 2020 event to the estimated interseismic rate can be reasonably neglected. After obtaining the LOS and azimuth interseismic displacement, we subtracted the secular components from the postseismic time series. Based on these corrected postseismic LOS and azimuthal measurements, we then calculated the postseismic east-west, north-south, and vertical displacements.

Viscoelastic modeling

We employed the PSGRN/PSCMP software[37] to model postseismic viscoelastic relaxation. This software requires a coseismic slip model as the driving force for postseismic deformation and divides the subsurface structure into multiple layers with laterally homogeneous parameters for each layer. Consequently, conventional modeling using this software cannot account for the lateral heterogeneities in both subsurface layering and viscosity coefficients across our study region for this earthquake. Our strategy involves separately determining the viscosity coefficients for the Arabian Plate and Anatolian Plate on either side of the fault, while maintaining the software's default homogeneous subsurface structure configuration. Through our experiments, we found that when determining the optimal viscosity coefficient for the Arabian Plate, we configured the software's subsurface layering to match the Arabian Plate's structure (Fig 1b). This configuration yielded optimal fitting between the forward-modeled surface deformation field and observations in the Arabian Plate region (south of the EAF) (Supplementary Fig. 18e), although the fit was suboptimal in the Anatolian Plate region (north of the EAF). Similarly, when determining the optimal viscosity coefficient for the Anatolian Plate, we aligned the software's subsurface layering with the Anatolian Plate's structure (Fig. 1b), achieving optimal fitting between modeled and observed surface deformation in the Anatolian Plate region (Supplementary Fig. 18f), despite poorer fitting in the Arabian Plate region. Supplementary Fig. 18 demonstrates the comparison between observations and modeled values when optimal fitting is achieved for each plate respectively. The results show distinct differences in fitting quality across the fault, while demonstrating relatively consistent fitting within the target plate.

To obtain a complete and optimal viscoelastic model-predicted deformation field, we spatially merged the deformation fields that achieved optimal fitting for the Arabian and Anatolian (Supplementary Figs. 18e and 18f). Specifically, we defined two normalized weight matrices, W_1 and W_2. For matrix W_1, the value is set to 1 at locations corresponding to the Arabian Plate (south of the EAF), decreases smoothly to 0 at locations north of the second seismic fault (i.e., Sürgü Fault), and transitions gradually between 1 and 0 in the intermediate region between the EAF and Sürgü Fault. The spatial characteristics of the W_1 matrix are illustrated in Supplementary Fig. 18b, and the W_2 matrix is simply defined as $W_2=1-W_1$ (Supplementary Fig. 18c). Let D_1 represent the optimal deformation field for the Arabian Plate region (Supplementary Fig. 18e) and D_2 the optimal deformation field for the Anatolian Plate (Supplementary Fig. 18f), the merged optimal deformation field D (Supplementary Fig. 18d) is then calculated through the weighted combination: $D = W_1*D_1 + W_2*D_2$ (where * denotes element-wise multiplication). Although we simply set the weighting factors between the two major earthquake ruptures to vary from 0 to 1, resulting in relatively larger modeling residuals within the transition region compared with areas outside the two major fault ruptures (Supplementary Fig. 5), the final merged displacement field is still able to capture the first-order postseismic deformation signals (Fig. 2).

We employed a grid search approach to determine the optimal viscosity parameters for the lower crust and upper mantle beneath both the Arabian and Anatolian plates. The search ranges and optimal values for each parameter are presented in Supplementary Tables 1 and 2. During the parameter optimization for both plates, we conducted forward modeling calculations for all possible parameter combinations to ensure comprehensive coverage of the parameter space.

In this study, the use of laterally homogeneous viscoelastic models to approximate a heterogeneous lithospheric structure implicitly assumes that postseismic viscoelastic flow beneath one side of the fault has a negligible influence on surface deformation on the opposite side. While we could avoid this assumption by using 3D finite element models, such models are computationally expensive and not well suited for extensive parameter-space exploration. However, to validate the reliability of this assumption, we performed a series of independent finite element simulations (using PyLith[82] see Supplementary Discussion 1) and demonstrate that the cross-fault influence of postseismic viscoelastic flow is negligible.

Poroelastic modeling

We use the coseismic slip model (Fig. 3a) and elastic half-space dislocation theory to compute vertical displacements associated with coseismic fault slip under undrained and drained Poisson's ratios (ν_u and ν_d). The difference between the two vertical displacement fields is taken as the forward model of poroelastic rebound. We fix ν_u=0.3 and vary the Poisson's ratio change $\Delta\nu = \nu_u - \nu_d$ from 0.01 to 0.2 with an increment of 0.01. For each $\Delta\nu$, we calculate the corresponding surface deformation field and compare the predicted and observed vertical displacements to identify the $\Delta\nu$ that best fits the observations.

In addition, lateral heterogeneity in the crust across the fault may lead to different poroelastic rebound responses on the two sides of the fault. Therefore, we adopt a strategy similar to that used in our viscoelastic modeling, estimating the optimal Poisson's ratio change on each side separately. This strategy is justified because, according to our poroelastic modeling framework, the poroelastic rebound deformation at a surface point depends only on the slip model, the location of the surface point, and the Poisson's ratio of the medium between the fault and that point. In other words, the Poisson's ratio on the opposite side of the fault has negligible effect on the rebound deformation on the side being evaluated. By independently comparing the predicted and observed rebound signals on both sides, we find that the optimal Poisson's ratio change $\Delta\nu$ is 0.13 for the Arabian plate and 0.1 for the Anatolian plate (Fig. 3d).

To quantitatively assess the sensitivity of Poisson's ratio changes constrained by the current InSAR vertical deformation data, we perform a synthetic experiment. We get the vertical deformation signal (Supplementary Fig. 19a) of the poroelastic rebound by using the Poisson's ratio change of 0.12, and add spatially correlated noise (Supplementary Fig. 19b), with a fractal dimension of 2.2 and an amplitude range of [-5 cm, 5 cm], to generate synthetic observations (Supplementary Fig. 19c). This type of noise is commonly used to simulate atmospheric artifacts in InSAR data[83] and can reasonably reproduce the residual signals present in real observations (Supplementary Fig. 5c). The chosen amplitude range ensures that the noise level is comparable to the misfit between the real data and model predictions (Fig. 3d). Applying the same search procedure as above yields one estimated Poisson's ratio change; repeating this process 10,000 times results in a variance of 0.015 for the estimated value (Supplementary Fig. 19d). We therefore conclude that the Poisson's ratio change constrained by the current InSAR data is 0.121±0.015, corresponding to a relative uncertainty of 12%.

Data availability

The Sentinel-1 data were downloaded from the Alaska Satellite Facility (https://vertex.daac.asf.alaska.edu/). The post-processed data presented in this study have been deposited in the Figsharedatabase at https://doi.org/10.6084/m9.figshare.29814851. The data supporting the findings of this study are provided in the Supplementary Information.

Code availability

All other calculation codes and examples used in this study are available on request from the corresponding author.

References

1. Bürgmann R, Dresen G. Rheology of the lower crust and upper mantle: Evidence from rock mechanics, geodesy, and field observations. *Annu. Rev. Earth Planet. Sci.* **36**, 531-567 (2008).
2. Freed AM, Lin J. Delayed triggering of the 1999 Hector Mine earthquake by viscoelastic stress transfer. *Nature* **411**, 180-183 (2001).
3. Nur A, Booker JR. Aftershocks Caused by Pore Fluid-Flow? *Science* **175**, 885-887 (1972).
4. Jonsson S, Segall P, Pedersen R, Bjornsson G. Post-earthquake ground movements correlated to pore-pressure transients. *Nature* **424**, 179-183 (2003).
5. Deng JS, Gurnis M, Kanamori H, Hauksson E. Viscoelastic flow in the lower crust after the 1992 Landers, Californial earthquake. *Science* **282**, 1689-1692 (1998).
6. Pollitz FF, Wicks C, Thatcher W. Mantle flow beneath a continental strike-slip fault: Postseismic deformation after the 1999 Hector Mine earthquake. *Science* **293**, 1814-1818 (2001).
7. Su LN, Shi FQ, Gan WJ, Su XN, Yan JY. Probing time-dependent afterslip and viscoelastic relaxation following the 2015 Mw7.8 Gorkha earthquake based on the 3-D finite-element model. *Earth Planets and Space* **72**, (2020).
8. Wang L, Wang R, Roth F, Enescu B, Hainzl S, Ergintav S. Afterslip and viscoelastic relaxation following the 1999 M7.4 Izmit earthquake from GPS measurements. *Geophys. J. Int.* **178**, 1220-1237 (2009).
9. Jin ZY, Fialko Y, Yang HF, Li Y. Transient Deformation Excited by the 2021 M7.4 Maduo (China) Earthquake: Evidence of a Deep Shear Zone. *J. Geophys. Res. Solid Earth* **128**, e2023JB026643 (2023).
10. Liu CL*, et al.* Complex multi-fault rupture and triggering during the 2023 earthquake doublet in southeastern Turkiye. *Nat. Commun.* **14**, 5564 (2023).
11. Jia Z*, et al.* The complex dynamics of the 2023 Kahramanmaraş, Turkey, Mw 7.8-7.7 earthquake doublet. *Science* **381**, 985-990 (2023).
12. Mai PM*, et al.* The destructive earthquake doublet of 6 February 2023 in south‐central Tü rkiye and northwestern Syria: Initial observations and analyses. *The Seismic Record* **3**, 105-115 (2023).
13. Taymaz T, Jackson J, Mckenzie D. Active tectonics of the north and central Aegean Sea. *Geophys. J. Int.* **106**, 433-490 (1991).
14. Taymaz T, Westaway R, Reilinger R. Active faulting and crustal deformation in the Eastern Mediterranean region. *Tectonophys.* **391**, 1-9 (2004).
15. Tapponnier P, Molnar P. Slip-Line Field-Theory and Large-Scale Continental Tectonics. *Nature* **264**, 319-324 (1976).

16. Şengör A, Görür N, Şaroğlu F. Strike-slip faulting and related basin formation in zones of tectonic escape: Turkey as a case study. *Strike-Slip Faulting and Basin Formation, edited by K. T. Biddle and N. Christie-Blick, Spec. Publ. SEPM Soc. Sediment. Geol.* **37**, 227-264 (1985).
17. Dewey JF, Hempton MR, Kidd WSF, Saroglu F, Sengör AMC. Shortening of continental lithosphere: the neotectonics of Eastern Anatolia - a young collision zone. *Geol Soc Spec Publ* **19**, 3-36 (1986).
18. Zhang L, Ding X, Lu Z. Modeling PSInSAR Time Series Without Phase Unwrapping. *IEEE Trans. Geosci. Remote Sens.* **49**, 547-556 (2011).
19. Toda S, Stein RS, Richards-Dinger K, Bozkurt SB. Forecasting the evolution of seismicity in southern California: Animations built on earthquake stress transfer. *Journal of Geophysical Research-Solid Earth* **110**, (2005).
20. Vanícek P, Krakiwsky EJ. *Geodesy: The Concepts*. Elsevier (1986).
21. Faccenna C, Becker TW, Jolivet L, Keskin M. Mantle convection in the Middle East: Reconciling Afar upwelling, Arabia indentation and Aegean trench rollback. *Earth Planet. Sci. Lett.* **375**, 254-269 (2013).
22. Faccenna C*, et al.* Mantle dynamics in the Mediterranean. *Rev. Geophys.* **52**, 283-332 (2014).
23. Roche V, Jolivet L, Papanikolaou D, Bozkurt E, Menant A, Rimmelé G. Slab fragmentation beneath the Aegean/Anatolia transition zone: Insights from the tectonic and metamorphic evolution of the Eastern Aegean region. *Tectonophysics* **754**, 101-129 (2019).
24. Whitney DL*, et al.* Breaking plates: Creation of the East Anatolian fault, the Anatolian plate, and a tectonic escape system. *Geology* **51**, 673-677 (2023).
25. Schildgen TF, Yildirim C, Cosentino D, Strecker MR. Linking slab break-off, Hellenic trench retreat, and uplift of the Central and Eastern Anatolian plateaus. *Earth Sci. Rev.* **128**, 147-168 (2014).
26. Okay AI, Zattin M, Özcan E, Sunal G. Uplift of Anatolia. *Turk. J. Earth Sci.* **29**, 696-713 (2020).
27. Mutlu AK, Karabulut H. Anisotropic Pn tomography of Turkey and adjacent regions. *Geophys. J. Int.* **187**, 1743-1758 (2011).
28. Karabulut H, Paul A, Özbakir AD, Ergün T, Sentürk S. A new crustal model of the Anatolia-Aegean domain: evidence for the dominant role of isostasy in the support of the Anatolian plateau. *Geophys. J. Int.* **218**, 57-73 (2019).
29. Kaviani A*, et al.* Crustal and uppermost mantle shear wave velocity structure beneath the Middle East from surface wave tomography. *Geophys. J. Int.* **221**, 1349-1365 (2020).
30. Berardino P, Fornaro G, Lanari R, Sansosti E. A new algorithm for surface deformation monitoring based on small baseline differential SAR interferograms. *IEEE Trans. Geosci. Remote Sens.* **40**, 2375-2383 (2002).
31. Liu J, Hu J, Burgmann R, Li Z, Sun Q, Ma Z. A Strain-Model Based InSAR Time Series Method and its Application to The Geysers Geothermal Field, California. *J. Geophys. Res. Solid Earth* **126**, e2021JB021939 (2021).
32. Li X*, et al.* Resolving the slip-rate inconsistency of the northern Dead Sea fault. *Sci. Adv.* **10**, eadj8408 (2024).
33. Li X, Jónsson S, Cao Y. Interseismic deformation from Sentinel-1 burst-overlap interferometry: Application to the southern Dead Sea fault. *Geophys. Res. Lett.* **48**, e2021GL093481 (2021).

34. Pollitz FF. Postearthquake relaxation evidence for laterally variable viscoelastic structure and water content in the Southern California mantle. *J. Geophys. Res. Solid Earth* **120**, 2672-2696 (2015).
35. Liu J, Jónsson S, Li X, Yao W, Klinger Y. Extensive off-fault damage around the 2023 Kahramanmaras earthquake surface ruptures. *Nat. Commun.* **16**, (2025).
36. USGS Earthquake Catalog, https://earthquake.usgs.gov/earthquakes/search/.
37. Wang RJ, Lorenzo-Martín F, Roth F. PSGRN/PSCMP: a new code for calculating co- and post-seismic deformation, geoid and gravity changes based on the viscoelastic-gravitational dislocation theory. *Comput. Geosci.* **32**, 527-541 (2006).
38. England P, Houseman G, Nocquet JM. Constraints from GPS measurements on the dynamics of deformation in Anatolia and the Aegean. *J. Geophys. Res. Solid Earth* **121**, 8888-8916 (2016).
39. Farr TG*, et al.* The shuttle radar topography mission. *Rev. Geophys.* **45**, (2007).
40. Magen Y*, et al.* Fault Coalescence, Slip Distribution, and Stress Drop of the February 2023 Southeast Turkiye Earthquakes from Joint Inversion of SAR, GNSS, and Burst Overlap Interferometry. *Seismol. Res. Lett.* **95**, 680-696 (2024).
41. Nergizci M*, et al.* Refining 3D Displacement Fields and Coseismic Slip Models of the 2023 Kahramanmaraş Earthquakes Using Subswath and Burst Overlap Interferometry (SBOI). *Journal of Geophysical Research-Solid Earth* **130**, e2025JB031421 (2025).
42. Nevada Geodetic Laboratory, MAGNET + Other GPS Networks Map, http://geodesy.unr.edu/NGLStationPages/gpsnetmap/GPSNetMap.html.
43. Ergintav S*, et al.* Unexpected far-field deformation of the 2023 Kahramanmaraş earthquakes revealed by space geodesy. *Science* **386**, 328-335 (2024).
44. Park S, Avouac JP, Zhan Z, Gualandi A. Weak upper-mantle base revealed by postseismic deformation of a deep earthquake. *Nature* **615**, 455-+ (2023).
45. Freed AM, Herring T, Bürgmann R. Steady-state laboratory flow laws alone fail to explain postseismic observations. *Earth Planet. Sci. Lett.* **300**, 1-10 (2010).
46. Ergintav S*, et al.* Seven years of postseismic deformation following the 1999, M=7.4 and M=7.2, Izmit-Duzce, Turkey earthquake sequence. *J. Geophys. Res. Solid Earth* **114**, B07403 (2009).
47. Li YC, Wang LF, Shan XJ, Zhao DZ. Spatiotemporal dominance of afterslip and viscoelastic relaxation revealed by four decades of post-1973 Luhuo earthquake observations. *Earth Planet. Sci. Lett.* **644**, 118949 (2024).
48. He LJ*, et al.* Coseismic kinematics of the 2023 Kahramanmaras, Turkey earthquake sequence from InSAR and optical data. *Geophys. Res. Lett.* **50**, e2023GL104693 (2023).
49. Ma ZF*, et al.* Space Geodetic Insights to the Dramatic Stress Rotation Induced by the February 2023 Turkey-Syria Earthquake Doublet. *Geophys. Res. Lett.* **51**, e2023GL107788 (2024).
50. Laske G, Masters G, Ma Z, Pasyanos M. Update on CRUST1. 0—A 1-degree global model of Earth's crust. In: *Geophysical research abstracts*) (2013).
51. Peltzer G, Rosen P, Rogez F, Hudnut K. Poroelastic rebound along the Landers 1992 earthquake surface rupture. *J. Geophys. Res. Solid Earth* **103**, 30131-30145 (1998).
52. Panuntun H, Miyazaki S, Fukuda Y, Orihara Y. Probing the Poisson's ratio of poroelastic rebound following the 2011 Mw 9.0 Tohoku earthquake. *Geophys. J. Int.* **215**, 2206-2221 (2018).
53. Hines TT, Hetland EA. Rapid and simultaneous estimation of fault slip and heterogeneous

lithospheric viscosity from post-seismic deformation. *Geophys. J. Int.* **204**, 569-582 (2016).

54. Peltzer G, Crampé F, King G. Evidence of nonlinear elasticity of the crust from the Mw7.6 Manyi (Tibet) earthquake. *Science* **286**, 272-276 (1999).
55. Fialko Y, Simons M, Agnew D. The complete (3-D) surface displacement field in the epicentral area of the 1999 M W 7.1 Hector Mine Earthquake, California, from space geodetic observations. *Geophys. Res. Lett.* **28**, 3063–3066 (2001).
56. Funning GJ, Parsons B, Wright TJ. Fault slip in the 1997 Manyi, Tibet earthquake from linear elastic modelling of InSAR displacements. *Geophys. J. Int.* **169**, 988-1008 (2007).
57. Liu SZ*, et al.* Lower Crustal Heterogeneity Beneath the Northern Tibetan Plateau Constrained by GPS Measurements Following the 2001 Mw7.8 Kokoxili Earthquake. *J. Geophys. Res. Solid Earth* **124**, 11992-12022 (2019).
58. Zhao D, Qu C, Bürgmann R, Gong W, Shan X. Relaxation of Tibetan lower crust and afterslip driven by the 2001 Mw7. 8 Kokoxili, China, earthquake constrained by a decade of geodetic measurements. *J. Geophys. Res. Solid Earth* **126**, e2020JB021314 (2021).
59. Liu J, Hu J, Buergmann R, Li Z, Jónsson S. Mitigating Atmospheric Delays in InSAR Time Series: The DetrendInSAR Method and Its Validation. *J. Geophys. Res. Solid Earth* **129**, e2024JB028920 (2024).
60. Li Z, Barbot S, Xiong W, Wang T. Fault properties and deep rheological structure over northeastern Bayankara block: revealed by post-seismic deformation following 2021 Mw 7.4 Maduo Earthquake. *AGU Fall Meeting Abstracts* **2023**, G23D-0507 (2023).
61. Helmstetter A, Shaw BE. Afterslip and aftershocks in the rate-and-state friction law. *Journal of Geophysical Research-Solid Earth* **114**, (2009).
62. Aharonov E, Scholz CH. The Brittle-Ductile Transition Predicted by a Physics-Based Friction Law. *Journal of Geophysical Research-Solid Earth* **124**, 2721-2737 (2019).
63. Pollitz FF. Transient rheology of the upper mantle beneath central Alaska inferred from the crustal velocity field following the 2002 Denali earthquake. *J. Geophys. Res. Solid Earth* **110**, (2005).
64. Fialko Y. Evidence of fluid-filled upper crust from observations of postseismic deformation due to the 1992 Mw7. 3 Landers earthquake. *J. Geophys. Res. Solid Earth* **109**, (2004).
65. Chen F*, et al.* Mechanism and implications of the post-seismic deformation following the 2021 Mw 7.4 Maduo (Tibet) earthquake. *Geophys. J. Int.* **237**, 203-216 (2024).
66. Sun T*, et al.* Prevalence of viscoelastic relaxation after the 2011 Tohoku-oki earthquake. *Nature* **514**, 84-87 (2014).
67. Freed AM, Bürgmann R, Calais E, Freymueller J. Stress-dependent power-law flow in the upper mantle following the 2002 Denali, Alaska, earthquake. *Earth Planet. Sci. Lett.* **252**, 481-489 (2006).
68. DeVries PMR, Krastev PG, Meade BJ. Geodetically constrained models of viscoelastic stress transfer and earthquake triggering along the North Anatolian fault. *Geochemistry Geophysics Geosystems* **17**, 2700-2716 (2016).
69. Çakir Z, de Chabalier JB, Armijo R, Meyer B, Barka A, Peltzer G. Coseismic and early post-seismic slip associated with the 1999 Izmit earthquake (Turkey), from SAR interferometry and tectonic field observations. *Geophys. J. Int.* **155**, 93-110 (2003).
70. DeVries PMR, Krastev PG, Dolan JF, Meade BJ. Viscoelastic Block Models of the North Anatolian Fault: A Unified Earthquake Cycle Representation of Pre- and Postseismic Geodetic Observations. *Bull. Seismol. Soc. Am.* **107**, 403-417 (2017).

71. Hearn EH, McClusky S, Ergintav S, Reilinger RE. Izmit earthquake postseismic deformation and dynamics of the North Anatolian Fault Zone. *J. Geophys. Res. Solid Earth* **114**, (2009).
72. Sunbul F, Nalbant SS, Simao NM, Steacy S. Investigating viscoelastic postseismic deformation due to large earthquakes in East Anatolia, Turkey. *J. Geodyn.* **94-95**, 50-58 (2016).
73. Sengör AMC, Özeren S, Genç T, Zor E. East Anatolian high plateau as a mantle-supported, north-south shortened domal structure. *Geophys. Res. Lett.* **30**, (2003).
74. Keskin M. Magma generation by slab steepening and breakoff beneath a subduction-accretion complex: An alternative model for collision-related volcanism in Eastern Anatolia, Turkey. *Geophys. Res. Lett.* **30**, 1-4 (2003).
75. Viltres R*, et al.* Present-day motion of the Arabian Plate. *Tectonics* **41**, e2021TC007013 (2022).
76. Castro-Perdomo N*, et al.* Interseismic deformation in the Gulf of Aqaba from GPS measurements. *Geophys. J. Int.* **228**, 477-492 (2022).
77. Bird P. Continental Delamination and the Colorado Plateau. *J. Geophys. Res.* **84**, 7561-7571 (1979).
78. Royden LH, Burchfiel BC, van der Hilst RD. The geological evolution of the Tibetan plateau. *Science* **321**, 1054-1058 (2008).
79. Wright TJ, Parsons BE, Lu Z. Toward mapping surface deformation in three dimensions using InSAR. *Geophys. Res. Lett.* **31**, 169-178 (2004).
80. Liu J*, et al.* Dynamic Estimation of Multi-Dimensional Deformation Time Series from InSAR Based on Kalman Filter and Strain Model. *IEEE Trans. Geosci. Remote Sens.* **60**, 1-16 (2022).
81. Cakir Z*, et al.* Arrest of the Mw 6.8 January 24, 2020 Elazig (Turkey) earthquake by shallow fault creep. *Earth Planet. Sci. Lett.* **608**, 118085 (2023).
82. Aagaard BT, Knepley MG, Williams CA. A domain decomposition approach to implementing fault slip in finite-element models of quasi-static and dynamic crustal deformation. *J. Geophys. Res. Solid Earth* **118**, 3059-3079 (2013).
83. Hanssen RF. *Radar Interferometry*. Springer Netherlands (2001).

Acknowledgements

We thank the European Space Agency (ESA) for providing free access to Sentinel-1 data and the Alaska Satellite Facility (ASF) for offering an efficient platform for data download. The large amount of InSAR data processing used for this paper was performed at the KAUST Ibex High Performance Computing (HPC). This work was supported by King Abdullah University of Science and Technology (KAUST), award BAS/1/1353-01-01 (SJ); ERC project, award BE_FACT-101142339 (YK).

Author contributions

Conceptualization: J.L. and S.J.; Investigation: J.L., S.J., X.L., W.Y., and Y.K.; Methodology: J.L., X.L.; Formal analysis: J.L., S.J., X.L., W.Y., and Y.K.; Visualization: J.L.; Resources: J.L., S.J., and Y.K.; Data curation: J.L.; Project administration: J.L.; Supervision: S.J. and Y.K.; Writing-original draft: J.L.; Writing-review and editing: J.L., S.J., X.L., W.Y., and Y.K.

Competing interests

The authors declare that they have no competing interests.

Editorial summary:
This study derives 3D surface displacement time series after the 2023 Kahramanmaraş earthquakes and shows that asymmetric temporal decay of deformation provides key evidence for contrasting viscoelastic relaxation as the dominant process.

Peer review information: *Nature Communications* thanks Yariv Hamiel, and the other, anonymous, reviewer(s) for their contribution to the peer review of this work. A peer review file is available.